

MOMENTUM-RESOLVED INVERSE PHOTOEMISSION

V. DOSE

*Max-Planck-Institut für Plasmaphysik, EURATOM Association,
D-8046 Garching/München, Fed. Rep. of Germany*

Manuscript received in final form 13 February 1986

Inverse photoemission including isochromat spectroscopy is shown to be a versatile technique to probe empty electronic states in solids and at clean and adsorbate covered surfaces. The complete set of quantum numbers of an electronic state can be determined and examples will be discussed for bulk and surface electronic states. For sufficiently low kinetic energy of the primary electrons, inverse photoemission is shown to be applicable to adsorbates also. This allows one to assess directly the unoccupied electronic states of the adsorbate which play an important role in the formation of the surface chemical bond. Examples are discussed for atomic and molecular chemisorption as well as adsorption on alkali promoted surfaces.

Contents

1. Introduction	339
1.1. Direct transitions	339
1.2. Photoemission versus inverse photoemission	340
2. Experimental techniques	342
2.1. Monochromators	342
2.2. Geiger counters	342
2.3. Merits and limitations	344
3. Bulk solids	344
3.1. Band mapping in mirror planes	344
3.2. Bulk bands of nickel	345
3.3. The two-band model	347
3.4. k -space location employing the nearly free electron approximation	349
3.5. k -space location by energy coincidence	350
3.6. Intensities	353
3.7. Band mapping along high symmetry lines	354
4. Surface states	355
4.1. Origin and nature of surface states	355
4.2. Temperature effects	356
4.3. Two-dimensional dispersion	358
4.4. Image potential states	359
4.5. The two-band model	360
4.6. Surface potential barrier	364
4.7. Surface scattering formalism	366
4.8. Effective masses	366
5. Chemisorption	367
5.1. Adsorption at solid surfaces	367
5.2. Atomic chemisorption	367
5.3. Molecular chemisorption	371
5.4. CO adsorption	375
Acknowledgements	377
References	377

1. Introduction

1.1. Direct transitions

Electrons impinging on a solid surface may emit radiation which is now known since ninety years [1] as X-ray emission. The electrons injected into the solid sample occupy previously empty electronic bands. Such excited states may decay via radiative transitions to other lower lying unoccupied electronic bands. An energy diagram for this process is depicted in fig. 1, which shows the case where two different radiative transitions from the same initial band are possible. Suppose the electrons impinging on the sample have a well-de-

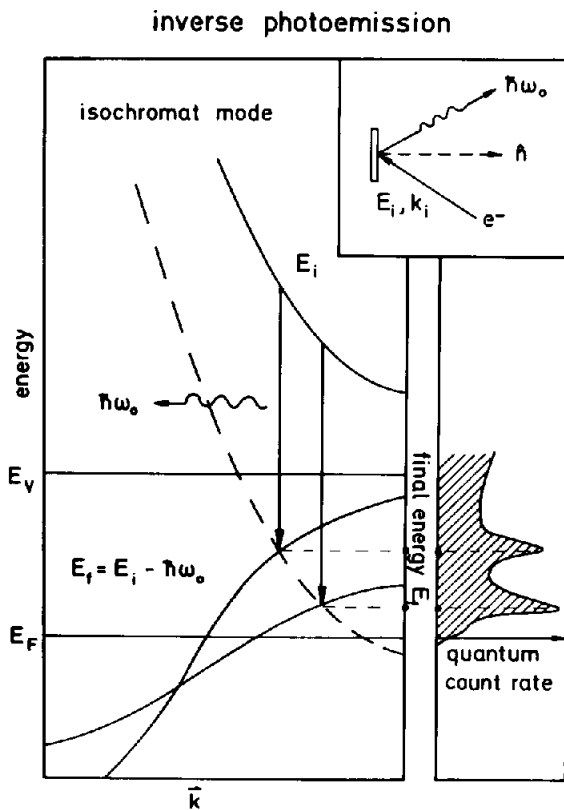


Fig. 1. Schematic of direct transitions in inverse photoemission. The dashed curve is the initial band shifted downward by the detection energy $\hbar\omega_0$. Its intersection with the lower lying final bands assigns final state energies and momenta to the peaks in the observed spectrum.

finer energy E_i and we measure the quantum energy of the emitted radiation $\hbar\omega$, we obtain by conservation of energy

$$E_f = E_i - \hbar\omega, \quad (1)$$

the energy of the final electronic state. Since this state has to be empty prior to the radiative transition E_f must lie above the Fermi energy of the solid.

The intensity distribution in the spectrum of emitted radiation is governed by the matrix element [2]

$$H_{if} \propto A_\sigma \langle E_f, \mathbf{k}_f, 1 | e^{i\mathbf{q} \cdot \mathbf{r}} \nabla V a_{q\sigma}^+ | E_i, \mathbf{k}_i, 0 \rangle. \quad (2)$$

The state vectors characterize energy and momentum of the electrons in the solid and the number of photons with wave vector \mathbf{q} and polarization σ in the radiation field. $a_{q\sigma}^+$ is the photon creation operator, V the bulk potential of the solid, and A_σ the vector potential amplitude. In monocrystalline solids V may conveniently be expressed in terms of a Fourier series over reciprocal lattice vectors \mathbf{G} .

$$V(\mathbf{r}) = \sum_{\mathbf{G}} V_{\mathbf{G}} e^{i\mathbf{G} \cdot \mathbf{r}}. \quad (3)$$

Let us further assume for a moment that the initial and final electronic state may be represented by free electron states to a reasonable degree. In such a case we obtain

$$H_{if} \propto A_\sigma \sum_{\mathbf{G}} V_{\mathbf{G}} \int e^{-i\mathbf{k}_f \cdot \mathbf{r}} e^{i\mathbf{q} \cdot \mathbf{r}} e^{i\mathbf{G} \cdot \mathbf{r}} e^{i\mathbf{k}_i \cdot \mathbf{r}} d\mathbf{r}, \quad (4)$$

which vanishes unless

$$\mathbf{k}_f - \mathbf{k}_i = \mathbf{G} + \mathbf{q}. \quad (5)$$

(5) expresses the momentum conservation for the radiative transition. In any realistic situation the initial state electron momentum \mathbf{k}_i can only be prepared with some uncertainty $\Delta\mathbf{k}_i$ and let us assume that $|\Delta\mathbf{k}_i| \approx 0.02 \text{ \AA}^{-1}$. We then find, that $|\mathbf{q}|$ may be neglected in the momentum balance as long as the photon energy stays below about 40 eV. This simplifies the momentum balance for photons in the ultraviolet range and has the important consequence that the initial and final wave vector of the electron differ only by a reciprocal lattice vector, in other words, in a reduced zone scheme the radiative transition occurs vertically. This is the famous direct transition concept [3], which forms the basis of band mapping in crystalline solids. A schematic representation is given in fig. 2.

1.2. Photoemission versus inverse photoemission

The foregoing discussion applies equally well to the case of light absorption. The matrix element for this case is instead of (2)

$$H_{if} \propto A_\sigma \langle E_f, \mathbf{k}_f, 0 | e^{i\mathbf{q} \cdot \mathbf{r}} \nabla V a_{q\sigma} | E_i, \mathbf{k}_i, 1 \rangle, \quad (6)$$

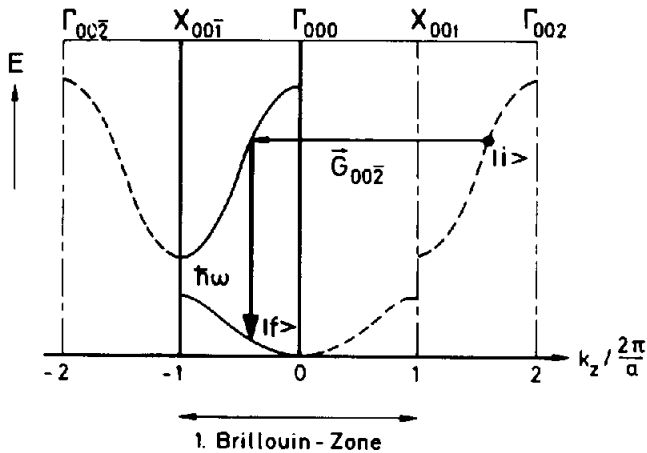


Fig. 2. Radiative transitions in a crystalline solid involve the exchange of a reciprocal lattice vector. In a reduced zone scheme they occur vertically, if the photon momentum is sufficiently small.

which differs from (2) in that the initial state is composed of an occupied electronic state and a radiation field with one photon of wave vector q and polarization σ , $a_{q\sigma}$ is the annihilation operator. (6) together with the conservation laws (1) and (5) forms the basis for the important technique of angular resolved photoemission (PES) [4]. The appellation inverse photoemission (IPE) for the related emission process emphasizes the intimate relationship of the two techniques. We shall finally point out their complementary nature. Since photoemission requires the excitation of an electron from an occupied initial band of the solid to an empty band from which the electron can escape into the vacuum in order to be analysed, its application is restricted to electronic states with energy below the Fermi energy E_F and above the vacuum energy E_V . Inverse photoemission requires two previously empty bands, one of which must lie above the vacuum energy E_V . The region $E_F < E \leq E_V$ is therefore the exclusive domain of inverse photoemission, the region $E < E_F$ is the exclusive domain of photoemission while the range $E > E_V$ is common to both techniques [5–10].

While the matrix elements (2) and (6) determine the intensity distribution within a given direct or inverse photoemission spectrum, the relation between the cross-sections for direct and inverse photoemission is governed by phase space factors [11–13], which make the inverse photoemission process for quantum energies in the ultraviolet less efficient by about $\alpha^2/2$, where α is Sommerfelds fine structure constant. This is an important point for the experimental realization of IPE.

2. Experimental techniques

2.1. Monochromators

IPE experiments date back to the early forties. They were performed in the 1 keV range using crystal monochromators and counters for the light detection. A modern experimental set-up of this type has been described by Lang and Baer [14]. The first experiment designed for operation in the ultraviolet with otherwise identical techniques was reported by Chauvet and Baptist [15]. They used a grazing incidence toroidal grating instrument covering the energy range from 20 to 100 eV. Since monochromators have a rather low acceptance such experiments are quite slow. An obvious improvement was first reported by Fauster et al. [16]. They employ multidetection techniques in their spectrometer. Their spectrograph is operated in normal incidence and two microchannel plate image intensifiers with resistive anodes tangent to the focal surface record the plus and minus first order diffracted spectrum thus covering the spectral ranges from 9–20 and 18–32 eV, simultaneously.

2.2. Geiger counters

The special impetus to IPE studies in the ultraviolet came, however, from an entirely different approach [17,18] which employed an energy selective Geiger–Müller counter in an IPE experiment. The counter has a CaF_2 entrance window and is filled with iodine and a noble gas. The energy selective properties of this detector result from a combination of the ultraviolet transmission characteristics of CaF_2 and the molecular photoionization yield of iodine. CaF_2 has a sharp transmission cut-off at 10.2 eV while iodine shows a step-like onset of photoionization at 9.2 eV. The combination provides a band-pass counter with 9.7 eV mean energy and a resolution of 800 meV (FWHM). Bremsstrahlung spectroscopy at fixed energy, hence at constant colour, is also frequently called isochromat spectroscopy. The rather low resolution has frequently been criticized. It has been shown recently that a substantial improvement to better than 400 meV can be obtained if SrF_2 is used as the entrance window [19].

The design of an actual IPE spectrometer based on the photon band-pass counter is shown in fig. 3 [20,21]. The counter is mounted in a standard UHV system equipped with the usual facilities for sample preparation and analysis. The sample can be rotated through 360° in the figure plane. It is shown in the IPE position opposite to a small electron gun mounted coaxially to a vacuum ultra-violet mirror. The gun is designed for low energy operation and delivers currents of the order of 10–20 μA at 10 eV with angular spread of about 5° . Radiation produced by electrons hitting the sample at a polar angle θ is imaged by the concave mirror into the band-pass counter opposite to the

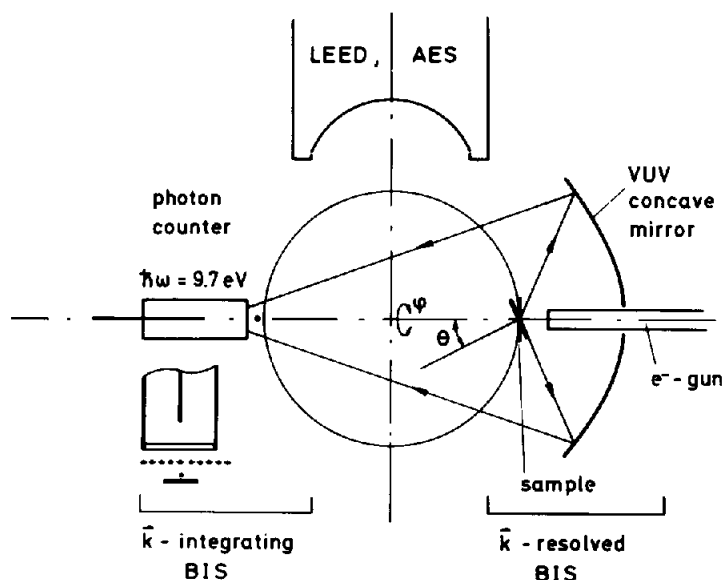


Fig. 3. Schematic of an apparatus for momentum resolved isochromat spectroscopy. An enlarged view of the detector position is given in the lower left corner.

mirror. The mirror is made from a glass blank by evaporation of aluminium and subsequent coating with magnesium fluoride [22].

An alternative IPE arrangement for normal incidence measurements is obtained by rotation of the sample through 180° in the figure plane. An enlarged view of the sample/counter geometry is given in the lower left corner of fig. 3. The electron source in this position is a simple tungsten filament. Due to the wide distribution of electron emission angles the spectra obtained approach the angle integrated case. A narrowing of this initial electron angular distribution can be achieved by negative bias on the grid behind the filament. This tends to bend the electrons towards the sample surface normal. The angular spread of the electrons for grid bias corresponding to the onset of space-charge effects has been estimated to be smaller than 15° [23].

The special value of this primitive assembly in combination with the gun/mirror set-up results from the different photon collection angles in the two positions. While the grid counter arrangement is predominantly sensitive to photon polarization parallel to the sample surface (A_x , A_y), the gun-mirror position has about equal sensitivities for all three vector potential components. A comparison of normal incidence spectra from the two positions will therefore reveal polarization effects which are in turn most useful for an identification of the orbital symmetry of states involved in the radiative transition [21].

2.3. *Merits and limitations*

Let us finally briefly comment on virtues and limitations of the different experimental approaches. Variable quantum energies offered by an UV spectrograph introduce a further highly desirable degree of freedom into an IPE experiment similar to synchrotron photoemission work. The counter approach on the other hand is exactly analogous to resonant lamp photoemission work. However, the bootstrap of fixed quantum energy of the photon counter experiment is largely compensated by a substantially higher sensitivity in terms of counts per coulomb charge deposited on the sample. Initial experience with the photon counter indicated a gain in sensitivity by four orders of magnitude compared to early crystal spectrographs [18]. Though modern large aperture VUV monochromators with multidetection narrow this initial gap considerably there remains a difference of by and large two orders of magnitude. This clearly favours the photon counter for studies of systems subject to beam damage [24]. It should also be mentioned that a counter spectrometer is cheap while the spectrograph approach requires substantial investments.

A recent monochromator design with limited tunability aims at the latter point. The chromatic imaging of a LiF lens in the energy range near the transmission cut-off where the dispersion is sufficiently rapid has been employed for variable quantum energy IPE work in the range 8–11 eV [25,26]. Since the optical acceptance of the lens was the same as that of the grating in [16] we expect similar sensitivities for both set-ups.

3. Bulk solids

3.1. *Band mapping in mirror planes*

We recall from section 1 that photoemission and inverse photoemission in the ultraviolet spectral range are suitable to determine the energy versus momentum dispersion $E(\mathbf{k})$ for occupied and empty electronic bands in crystalline solids. Such dispersion relations are of fundamental importance for the description of crystalline solids and provide the input information for the calculation of many macroscopic properties such as magnetic, transport and optical properties.

Since the band structure of even simple crystals is quite complicated at general points in momentum space actual experiments are usually carried out in mirror planes. Fig. 4 shows the Brillouin zone of an fcc lattice. The shaded planes are the ΓXUL and ΓXWK mirror planes of the crystal. Working in mirror planes has several advantages. Different bands may become degenerate in mirror planes. The complexity of the observed spectra is therefore reduced. Because of symmetry the bands cross mirror planes with zero slope. This

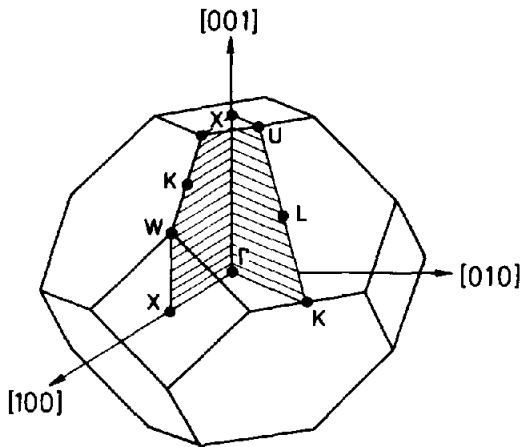


Fig. 4. The brillouin zone of a face centered cubic crystal.

property may be explored for a proper positioning of the crystal in an actual experiment or as a method for absolute k -space location in certain cases [27]. Further, special polarization selection rules apply for experiments in mirror planes. The solution of Schrödinger's equation must be of odd or even parity under reflection in a mirror plane. The wavefunction of the electron in an IPE experiment approaching the crystal surface is a plane wave and has therefore even parity. It can couple only to those bulk electronic wavefunctions which have also even parity. Consider now the transition matrix elements (2). Clearly the integrant must be even under reflection in order to give a non-zero value. If we write (2) in shorthand as

$$H_{if} \propto A_{\parallel} \langle f | (\nabla V)_{\parallel} | i \rangle + A_{\perp} \langle f | (\nabla V)_{\perp} | i \rangle, \quad (7)$$

where \parallel and \perp refer to the mirror plane, we see immediately that emission with polarization in the mirror plane results from transitions into final states with even parity while emission with polarization perpendicular to the mirror plane results from final states with odd parity. This leads again to a reduction of the number of energetically possible transitions and a concomitant simplification of the observed spectra.

3.2. Bulk bands of nickel

Fig. 5 shows experimental IPE spectra obtained with the spectrometer in fig. 3 [19]. The only variable in work with fixed detection energy is the energy of the incident electron and the only parameter the angle of incidence with respect to the surface normal. The left panel in fig. 5 shows the spectra for a variation of the polar angle of incidence θ in the ΓXWK plane. The data

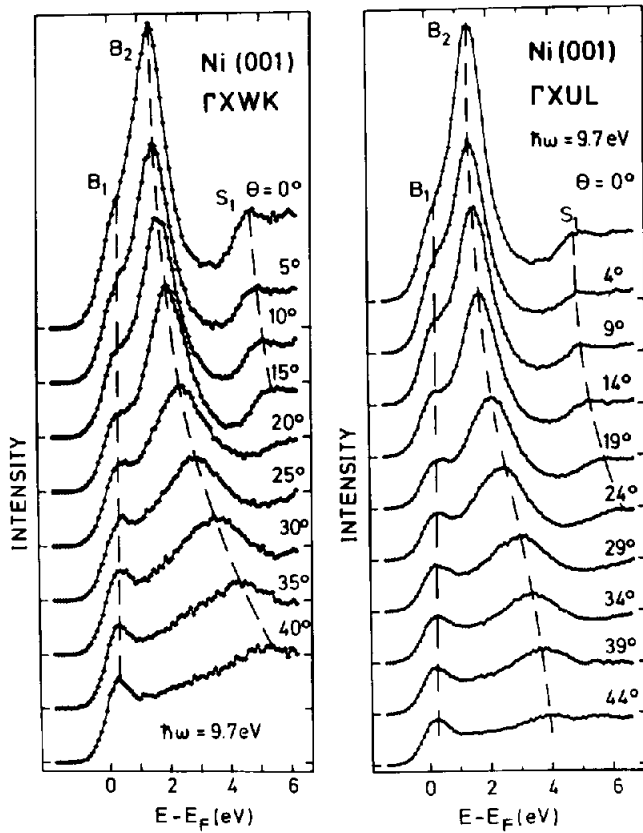


Fig. 5. Isochromat spectra from Ni(001) at various polar angles θ in the two bulk mirror planes. The dashed lines show the dispersions of two bulk and one surface state.

represent the intensity of the observed radiation as a function of final state energy E_f . Three different emission features are present. Right at the Fermi energy we observe a peak B_1 which remains stationary upon variation of the polar angle. It will be shown to be due to empty d-bands. Peak B_2 , starting at 1.4 eV for normal incidence on the other hand, exhibits rapid dispersion and will be shown to be due to transitions between sp-like bands. A step like emission S_1 around 4.5 eV shows also some dispersion. It is due to transitions into surface states and will be discussed further in section 4.

Spectra for the ΓXUL mirror plane are shown in the right-hand panel of fig. 5 [19]. They are by and large similar to those for ΓXWK except for a noticeably smaller dispersion of peak B_2 at larger angles.

We shall now try to derive energy versus momentum dispersion from the observed data. This encounters some difficulties because the electron wavevec-

tors \mathbf{k} involved in (5) refer to the bulk solid while the initial conditions of the experiment specify only the wavevector \mathbf{K} in vacuum. But \mathbf{k}_i is certainly different from \mathbf{K}_i because the incident electron experiences a force of unknown magnitude normal to the surface due to the vacuum solid boundary. The forces parallel to the surface are periodic and lead to diffraction such that

$$\mathbf{k}_{i\parallel} = \mathbf{K}_{i\parallel} + \mathbf{g}_{\parallel}, \quad (8)$$

where \mathbf{g}_{\parallel} is a surface reciprocal lattice vector. At sufficiently low quantum energy and hence initial energy the requirement that

$$|\mathbf{k}_{i\parallel} - \mathbf{g}_{\parallel}| \leq |\mathbf{K}_i| \quad (9)$$

leads to a preference for $\mathbf{g}_{\parallel} = 0$. $|\mathbf{K}_{i\parallel}|$ is on the other hand given by

$$K_{i\parallel} = \left[2m(E_f + \hbar\omega - \phi_p)/\hbar^2 \right]^{1/2} \sin \theta, \quad (10)$$

where E_f is the final state energy with respect to the sample Fermi level and ϕ_p is the sample work function. A plot of the experimental data for both mirror planes in terms of $E_f(\mathbf{k}_{\parallel})$ is given in fig. 6. Solid dots labeled B_1 , B_2 and S_1 refer to corresponding emission features in fig. 5. Emissions S_2 , B_3 , B_4 are outside the range of the data reproduced in fig. 5. The areas surrounded by shaded boundaries are the gaps of the projected bulk band structure from a theoretical calculation. For $(E, \mathbf{k}_{\parallel})$ combinations inside these boundaries no bulk electronic states are available. Since emissions S_1 , S_2 occur in such gaps, they must be due to surface states and will be further discussed in section 4. A comparison between experiment and the theoretical band structure calculation can be obtained in terms of "optical curves" for a transition energy of $\hbar\omega = 9.7$ eV. These are shown as dashed lines and represent the final state $E_f(\mathbf{k}_{\parallel})$ for any pairs of bands 9.7 eV apart at the same \mathbf{k}_{\parallel} irrespective of the associated value of \mathbf{k}_{\perp} . The experimental data fall close to such curves but only a minority of optical curves is observed experimentally. This is a consequence of matrix-element effects either in terms of selection rules or due to a small overlap between the incident free electron wave with the initial state bulk Bloch wave. This overlap is strongest for bands with nearly free electron character.

3.3. The two-band model

Let us consider in more detail the rapidly dispersion bulk transition B_2 . The measured data follow quite well a dispersion relation

$$E(\mathbf{k}_{\parallel}) = E_0 + (\hbar^2/2m)k_{\parallel}^2, \quad (11)$$

with $E_0 = 1.55$ eV. This relation is shown as a dashed line in fig. 6. Such a behaviour may be derived assuming that the transition occurs between free-

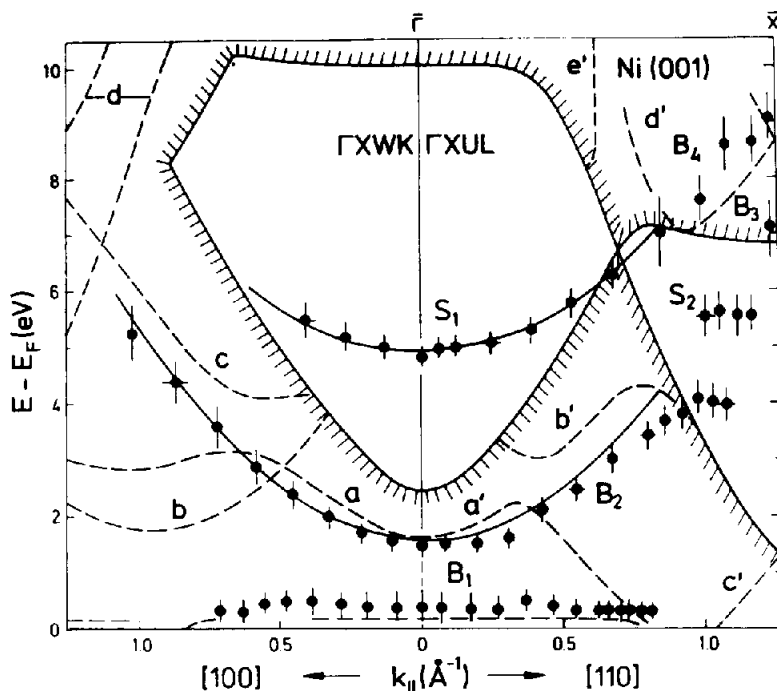


Fig. 6. Final state energies ($E - E_F$) as a function of k_{\parallel} for iso-chromat emission peaks observed from Ni(001). The electrons impinged in the Γ XWK (left side) and Γ XUL (right) bulk mirror planes, respectively. Dashed lines indicate kinematically allowed bulk direct transitions. Unshaded areas mark gaps of the projected bulk band structure.

electron-like bands [28]. Suppose the hybridization with other bands, in particular d-bands, may be neglected and a two-band approximation based on the two plane waves $\exp(i\mathbf{k} \cdot \mathbf{r})$ and $\exp[i(\mathbf{k} - \mathbf{G}) \cdot \mathbf{r}]$, where \mathbf{G} is an appropriate reciprocal lattice vector, applies. Let V_G represent the pseudopotential coefficient through which the two plane waves interact.

$$V(\mathbf{r}) = V_G [\exp(i\mathbf{G} \cdot \mathbf{r}) + \exp(-i\mathbf{G} \cdot \mathbf{r})]. \quad (12)$$

Using the trial function

$$\psi_t(\mathbf{r}) = a \exp(i\mathbf{k} \cdot \mathbf{r}) + b \exp[i(\mathbf{k} - \mathbf{G}) \cdot \mathbf{r}], \quad (13)$$

the variation principle leads to the matrix equation

$$\begin{pmatrix} \hbar^2 k^2 / 2m - E & V_G \\ V_G & \hbar^2 (\mathbf{k} - \mathbf{G})^2 / 2m - E \end{pmatrix} \times \begin{pmatrix} a \\ b \end{pmatrix} = 0. \quad (14)$$

This has a solution when

$$(\hbar^2 k^2 / 2m - E) [\hbar^2 (\mathbf{k} - \mathbf{G})^2 / 2m - E] - V_G^2 = 0. \quad (15)$$

Let $E_k = \hbar^2 k^2 / 2m$ and $E_{k-G} = \hbar^2 (\mathbf{k} - \mathbf{G})^2 / 2m$ then

$$2E_i = (E_{k-G} + E_k) + [(E_{k-G} - E_k)^2 + 4V_G^2]^{1/2}, \quad (16)$$

$$2E_f = (E_{k-G} + E_k) - [(E_{k-G} - E_k)^2 + 4V_G^2]^{1/2}. \quad (17)$$

Optical transitions at $\hbar\omega$ are defined by (1) which leads to

$$(\hbar^2/m)\mathbf{k} \cdot \mathbf{G} = [(\hbar\omega)^2 - 4V_G^2]^{1/2} - E_G, \quad (18)$$

with $E_G = \hbar^2 G^2 / 2m$. (18) defines a plane in \mathbf{k} -space normal to \mathbf{G} . Let k_{\parallel} and k_{\perp} be the components of \mathbf{k} parallel and normal to this plane (and therefore normal and parallel to \mathbf{G} , respectively). The simultaneous solution of (16)–(18) yields then

$$E_f(k_{\parallel}) = \hbar^2 k_{\parallel}^2 / 2m + [(E_G - \hbar\omega)^2 - 4V_G^2] / 4E_G. \quad (19)$$

The dispersion in this approximation is perfectly free electron like in k_{\parallel} in agreement with the experimental data. This brings us back to fig. 6. Transition B_2 is seen to follow the optical curves (a') and (b') derived from a theoretical band structure calculation only in those intervals of k_{\parallel} where (a') and (b') behave free-electron-like. This is because the initial state wavefunction is no longer well represented by a single plane wave outside these ranges, in other words the overlap becomes small. Similar considerations apply to optical curves (a) and (c) in the Γ XWK plane. The fact that in neither mirror plane the gap between (a'), (b') and (a), (c) is reflected in the experimental data must be attributed to appreciable lifetime broadening of the final electronic band. In fact the line width of B_2 is about 1.3 eV independent of the choice of experimental resolution [19].

3.4. \mathbf{k} -space location employing the nearly free electron approximation

Though we have certainly expounded the information contained in the experimental spectra of fig. 5 we are left with the unpleasant situation that a single experiment does not reveal the three-dimensional $E(\mathbf{k})$ information we were hunting for. This can be obtained in an approximate way assuming a nearly free electron dispersion for the initial band [4]. In this approximation the bulk solid is represented by a structureless potential trough of depth $|V_0| + \phi_p$. From (1) we have

$$E_i = \hbar\omega + E_f = E_{\text{kin},i} - |V_0|, \quad (20)$$

$$E_{\text{kin},i} = \hbar\omega + E_f + |V_0| = \hbar^2 (k_{\parallel}^2 + k_{\perp}^2) / 2m, \quad (21)$$

which defines a circle in the $(k_{\parallel}, k_{\perp})$ plane for a given state energy. Fig. 7 shows the Γ XWK mirror plane of the fcc Brillouin zone with constant energy circles corresponding to final state energies read from the B_2 peak position in

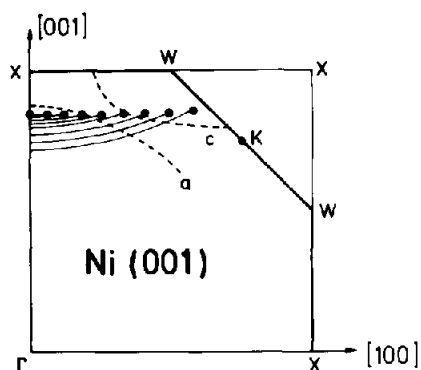


Fig. 7. k -space location of an observed direct transition employing the free electron initial state approximation.

fig. 5. The intersection with the parallels to ΓX defined by eq. (10) are shown as full dots and represent the three-dimensional k -space location of the observed transition in the free electron initial state approximation. From the fact that they run parallel to the zone boundary we conclude with the help of (18) that the reciprocal lattice vector exchanged in the transition is in the $\{001\}$ direction. The optical curves (a) and (c) from a band structure calculation are also included (see also fig. 6) in order to reveal virtues and shortcomings of the nearly free electron initial state approximation.

3.5. k -space location by energy coincidence

The nearly free electron approximation has enjoyed widespread application in angular resolved photoemission spectroscopy due to its apparent simplicity. However, direct methods to determine the unknown momentum component k_{\perp} by two independent measurements have been proposed quite early. The triangulation or energy coincidence method originally proposed by Kane [29] requires the observation of a given interband transition from two differently oriented surfaces. By this way we obtain two momenta k_{\parallel} with respect to the two different surface normals for the same point in k -space. Fig. 8 [19] shows a series of spectra from Ni(111) for angles of incidence $\theta^{(111)}$ between 0° and 45° in the $\Gamma L K L$ mirror plane. A similar series of spectra was obtained from Ni(110) for angles of incidence $\theta^{(110)}$ between 2° and 47° . The 2° spectrum out of this series is shown in the lower panel of fig. 8. Comparing this spectrum with the series from the (111) surface we find that the B_3 transition occurs on the (111) surface at the same energy for $\theta^{(111)} = 45^\circ$ and exhibits the same line width. This leads us to suspect that B_3 for $\theta^{(110)} = 2^\circ$ and $\theta^{(111)} = 45^\circ$ occurs in

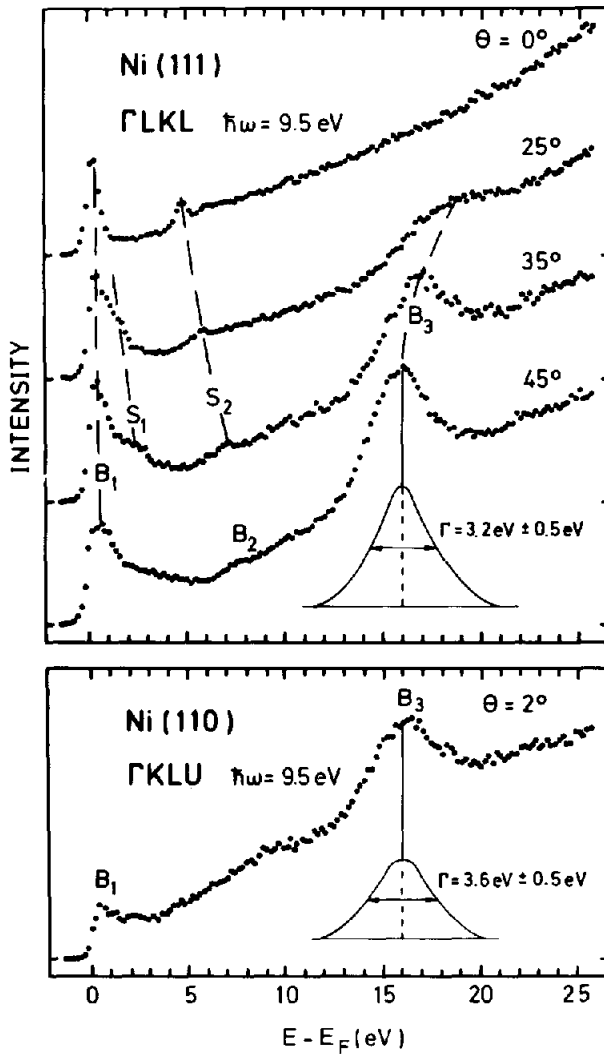


Fig. 8. Energy coincidence between the B_3 transition observed at 2° on Ni(110) and the B_3 transition observed at 45° on Ni(111) suggests, that the final state $E_f(k_f)$ is the same in both cases.

fact at the same point in k -space. An $E(k_{||})$ representation of all the available results is given in the lower part of fig. 9. In a first step of data reduction the nearly free electron initial state approximation has been employed to obtain a three-dimensional k -space location. The result is shown in the upper part of

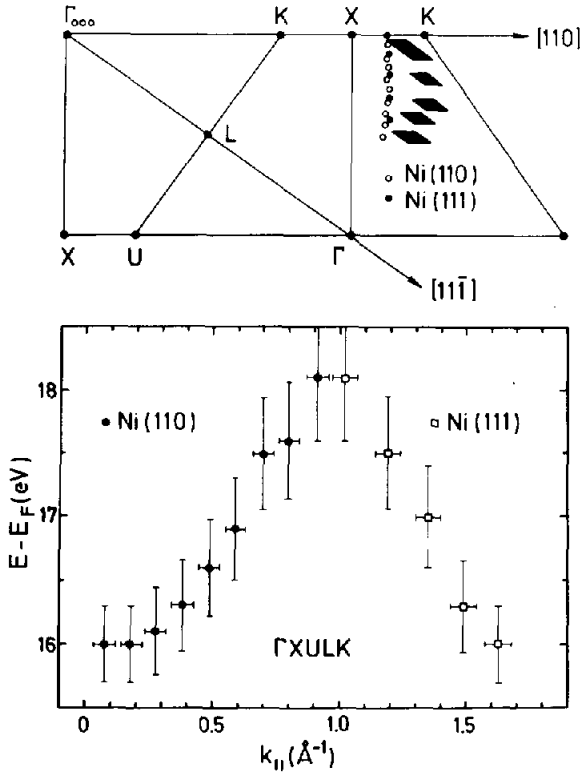


Fig. 9. Solid dots and open squares represent the experimentally determined $E(k_{||})$ for the B_3 transition on Ni(110) and Ni(111), respectively (see fig. 8). Solid dots and open circles in the upper part represent the k -space location in the free electron initial state approximation. Solid diamonds are obtained by triangulation.

fig. 9 as open circles for the (110) plane and full dots for the (111) plane. The coincidence of the two sets in k -space lends further support to the assumption that the same transition is in fact observed from the two crystal surfaces. k -space location without resorting to the free electron approximation proceeds as follows. We select a pair of data satisfying $E_f(k_{||}^{(110)}) = E_f(k_{||}^{(111)})$. The associated values of $k_{||}^{(110)}$ and $k_{||}^{(111)}$ define parallels to the ΓK and ΓL directions, respectively, whose intersection is marked by the full diamonds in fig. 9. These diamonds represent now the full three-dimensional experimental energy band dispersion obtained without resorting to any auxiliary information. The size of the diamonds indicates experimental uncertainty. In spite of this relatively large error fig. 9 shows that the free-electron approximation may be considerably in error even at such high energies.

3.6. Intensities

The analysis of data so far described has only made use of the conservation laws (1) and (5). This has provided a satisfactory understanding of energy momentum dispersion of bulk electronic states. A more advanced theory would also aim at an understanding of intensities. To this end an explicit evaluation of the matrix element (2) is necessary. In the spirit of the three-step model of inverse photoemission the initial and final electronic states are then bulk Bloch waves. The penetration of the electron from vacuum into the solid sample and the competition between radiative and non-radiative decay have to be introduced in addition, in order to describe the observed intensities [28]. This three-step bulk direct transition model has the advantage of great transparency. The incoherent treatment of penetration, transport and optical de-excitation and the inability to describe surface electronic states remain however unsatisfactory. A theoretically much more satisfactory, though physically less transparent approach to the description of intensities in inverse photoemission spectra has been formulated by Pendry [13,30]. This treatment is also frequently called the one-step theory of inverse photoemission. The electronic states entering the one-step theory are LEED states which incorporate the effects of transport and penetration coherently. Explicit calculations for Ni(001) are available from the work of Thörner and Borstel [31]. Their calculations are based on the potential generated by Moruzzi et al. [32]. An absorptive part of

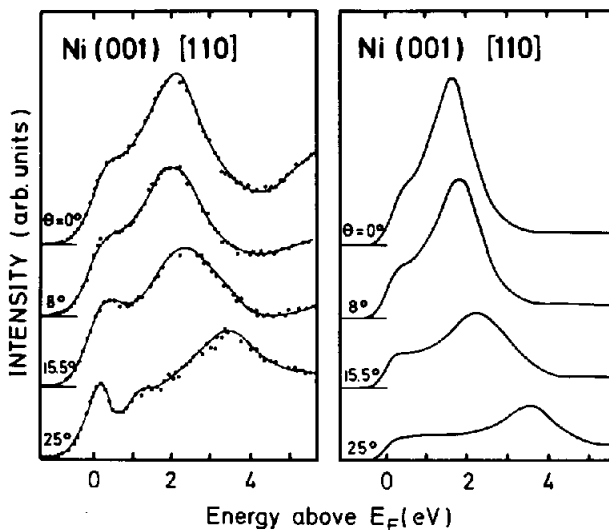


Fig. 10. A fully dynamical one step theory of inverse photoemission reproduces quite well not only energetic positions but also intensities of the observed spectra.

-0.4 eV was added to the potential for the final states. For the initial bands, an absorptive part of -0.75 eV was used. A rectangular surface barrier representing a workfunction of 5.1 eV was placed at 0.8 interlayer distances outside the outermost atomic layer. Fig. 10 shows a sample of their spectra after convolution with a Gaussian in order to account for the finite experimental resolution in comparison to experimental data. The agreement is considered to be excellent.

3.7. Band mapping along high symmetry lines

It was already pointed out in section 2 that variable quantum energy introduces another highly desirable degree of freedom into inverse photoemission experiments. This is particularly true for the mapping of bulk energy bands. Consider, for example, the case where the detection energy is smaller than the band gap at the zone boundary in fig. 1. No emission would be observable in such a case no matter what initial energy E_i we choose. Only by increasing the quantum energy and simultaneously matching the initial state energy E_i a spectrum is obtained which can now be traced in momentum space until the final bands dive below the Fermi energy. The special advantage of keeping the direction in momentum space constant is that this direction can be chosen along high symmetry lines. A knowledge of the band structure along all high symmetry lines on the other hand implies the band structure in the whole Brillouin zone [33].

As an example for band mapping along high symmetry lines we refer to an inverse photoemission study of GaAs(110) [34]. For normally incident electrons the momentum is along $\Gamma\Sigma\text{KSX}$ and is determined using the initial state free electron approximation. The initial state energy was varied between 12.25 and 28.25 eV. The resulting energy versus momentum dispersion is shown in fig. 11. Interestingly the whole set of data could only be understood if in addition to $\mathbf{g}_{\parallel} = 0$ in (8) also $\mathbf{g}_{\parallel} = (\bar{1}, 1, 1)$ and $\mathbf{g}_{\parallel} = (0, 0, \bar{2})$ were considered. The occurrence of such "umklapp" processes is certainly favoured by the large unit cell in real space and the associated small reciprocal lattice vectors in momentum space. The horizontal line marked SS denotes an emission feature which remains stationary upon variation of the momentum normal to the surface. Such a behaviour is expected for an electronic surface state, which can exhibit only two-dimensional dispersion with \mathbf{k}_{\parallel} .

Two-dimensional dispersion of energy bands is also most frequently observed in layered materials such as graphite and its intercalation compounds [35] and transition metal dichalcogenides [36]. These materials are characterized by covalently bound sheets of atoms which interact with each other only weakly through Van der Waals forces. In theoretical descriptions the sheets are frequently considered as isolated to a first approximation and the effects of interlayer interaction are then treated as weak perturbations. In an

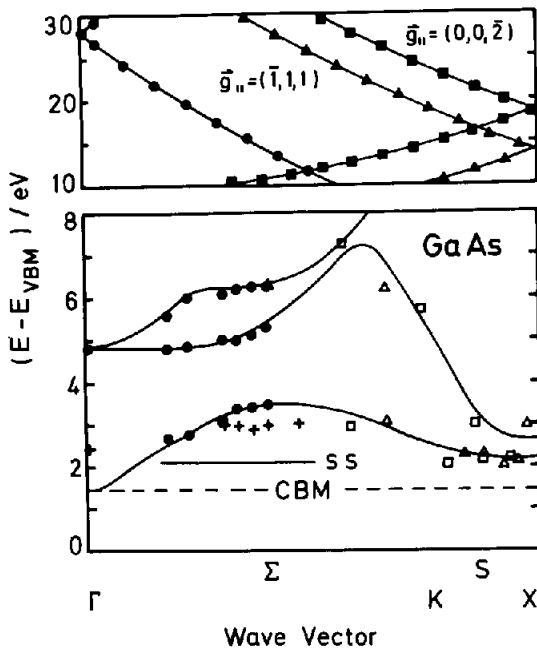


Fig. 11. Variable quantum detection energy permits band mapping along high symmetry lines. The momentum associated with the observed final state energies was derived from the free electron initial state approximation [34]. Solid lines in the lower panel represent a theoretical band structure.

inverse photoemission study of graphite and stage one lithium intercalated graphite Fauster et al. [35] were able to distinguish electronic bands due to in-layer and interlayer interactions. While the energies of in-layer bands remain stationary upon variation of k_{\perp} through variation of the detection energy, the energies of bands due to interlayer interaction clearly show dispersion with k_{\perp} .

4. Surface states

4.1. Origin and nature of surface states

The termination of a solid by a surface breaks its three-dimensional symmetry, changes the co-ordination number of the surface atoms as compared to atoms in the bulk and may therefore give rise to various modifications of the electronic and concomitantly geometrical structure. Electronic wavefunctions need no longer be periodic in the direction of the surface normal. This introduces electron states forbidden in an infinite crystal. Such states are called surface states or surface resonances depending on their

detailed physical origin. Surface states can have a very different character depending on their concentration near the surface and the strength of the surface potential. d-like surface states in transition metals have atomic like localized wavefunctions. These states are split off into a gap from bulk bands by the surface potential. Their existence requires that the surface perturbation of the one electron potential is sufficiently strong compared with the band width. Such states are usually called "Tamm" states [37] and may be visualized as a band bending effect over the distance of one atomic layer. sp-like surface states arise primarily from new boundary conditions introduced by the surface. These Shockley states [38] may extend deeper into the solid. Angle-resolved photoemission has revealed a considerable number of occupied surface bands and determined their energy dispersion and symmetry character. Inverse photoemission of empty surface states has turned out to be a similarly attractive area for study.

A property common to all electron spectroscopic methods in surface physics is that they reveal simultaneously bulk and surface properties. Additional diagnostic means are therefore necessary in order to discriminate between bulk and surface features in the observed spectra. Fig. 12 shows a series of inverse photoemission spectra from Cu(110) at $\hbar\omega = 9.7$ eV. The uppermost trace is obtained from the clean surface. Following the common practice of ordinary photoemission the sample was then exposed to various amounts of oxygen. The expectation is, that electronic surface states respond sensitively to adsorption of gas. This is in fact the observed behaviour of peak S whose intensity decreases rapidly as a function of oxygen exposure until it is fully quenched at already 5 L (1 L = 1 langmuir = 10^{-6} Torr s = 1.3×10^{-4} Pa s). Quite a different behaviour is exhibited by the peak right at the Fermi level, it is nearly unaffected by the adsorbed oxygen. This is what we expect from a bulk transition. Caution must be exercised, however. A gaseous layer adsorbed on the surface can alter significantly the amount of coupling between the incident free-electron wave and bulk bloch waves and thereby attenuate also bulk direct transitions. The effect can be strong enough to lead to erroneous assignments [39,40]. Let us finally briefly comment on peak A in fig. 12. Oxygen adsorption on Cu(110) leads to an ordered (2×1) overlayer. Faint indications of this superstructure are already visible after an exposure of only 1 L. It sharpens with increasing exposure until a sharp low background LEED picture is seen. The oxygen exposure manifests itself in the inverse photoemission spectrum through peak "A" which results from radiative transitions into oxygen induced electronic states. A detailed discussion of adsorbate induced states shall be postponed to section 5.

4.2. Temperature effects

Another approach to discriminate between bulk and surface features in inverse photoemission spectra is the investigation of their temperature depend-

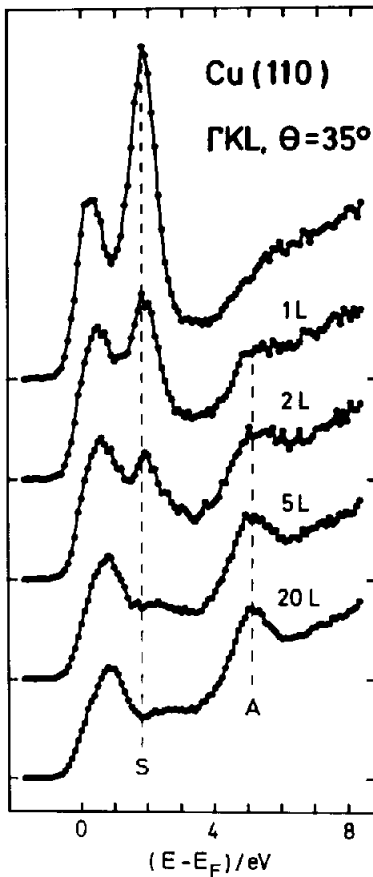


Fig. 12. Isochromat spectra taken from Cu(110) pre-exposed to various doses of oxygen show the quenching of the surface state emission "S" and the simultaneous development of an adsorbate induced emission feature "A".

ence [41]. Though the scattering of electrons by phonons is quasi-elastic it is associated with a considerable change of the electron momentum. This means that electron phonon interaction tends to randomize the electron momentum and thereby attenuates direct transition features as the sample temperature rises. The difference between bulk and surface electronic states is that surface Debye temperatures are lower than bulk values because of the reduced co-ordination number of the surface atoms. We therefore expect that surface features respond more sensitively to temperature increases than bulk direct transitions. An example is given in fig. 13. The increase of the sample temperature from 320 to 570 K results in a considerable attenuation of the

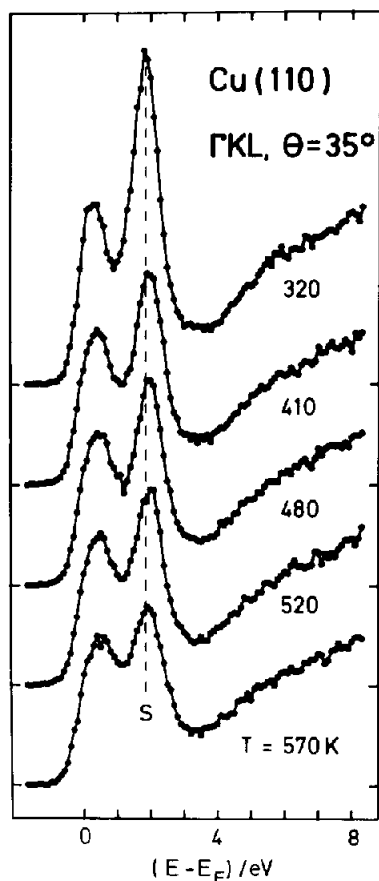


Fig. 13. The surface emission feature "S" on Cu(110) is considerably attenuated at elevated temperatures while the bulk direct transition near the Fermi level remains nearly unaffected.

surface feature S while the bulk state right at the Fermi level is nearly unaffected similar to the response to oxygen adsorption. In fact if we assume a simple exponential temperature dependence of the emission intensities

$$I = I_0 \exp(-T/T_C), \quad (22)$$

we find $T_C = 3.7 \times 10^3$ K for the bulk transition and $T_C = 580$ K for the surface emission feature.

4.3. Two-dimensional dispersion

We have already mentioned in section 3 that the energy of surface states shows only two-dimensional dispersion. A very stringent test for the surface origin of a particular emission feature is therefore that for normal incidence of

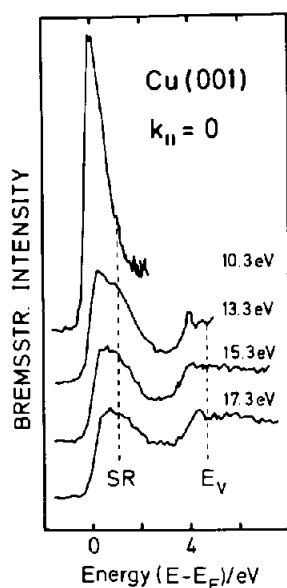


Fig. 14. Inverse photoemission spectra for electrons normally incident on Cu(001) for various initial state energies E_i . The bulk direct transition observed close to E_F for $E_i = 10.3$ eV is no longer excited at higher energies. Surface emission features from image potential states near E_v and a surface resonance at SR, however, remain stationary upon variation of the quantum detection energy.

the initial state electrons the final state should remain stationary upon a variation of k_\perp by tuning of the detection quantum energy. An example of this technique is given in fig. 14 [42] which shows a series of spectra from Cu(001) for quantum energies between 10.3 and 17.3 eV. At 10.3 eV we see a bulk direct transition right at the Fermi energy which originates from similar bands as B_2 in fig. 5. This emission vanishes as the detection energy is raised. The step-like emission feature slightly below the vacuum level E_v , however, remains unaffected. A similar feature in the nickel spectra of fig. 5 exhibited dispersion with k_\parallel and occurred only in a bulk band gap. This is also a sufficient though not necessary condition of a surface state. The rigorous condition for a surface state is that it may not coincide with bulk states of the same E , k_\parallel and symmetry. This prevents mixing of bulk and surface functions which would lead to what we call a surface resonance.

4.4. Image potential states

While the behaviour of surface states as discussed in the previous paragraph is well-known from conventional photoemission spectroscopy we shall now

turn to phenomena associated with surface states which have no occupied predecessor. It will be shown later that this second class of surface states arise from the long range image potential experienced by an electron in front of a metal surface. Such image potential states manifest themselves in inverse photoemission spectra by a step-like emission feature slightly below the vacuum level, see fig. 14. They have so far been observed on many metal surfaces [41–46]. The response of the image potential feature to gas adsorption and temperature treatment is entirely different from that discussed in section 4.1. For emission from Cu(001) it could be shown that the intensity of the image potential emission remained unaltered when the sample temperature was increased to 900 K [41]. The bulk direct transition was attenuated by more than 30% at the same time. The conclusion from this observation was that the wavefunctions of the image potential states must peak well outside the surface in the vacuum because of the observed insensitivity to surface vibration. A similarly unusual behaviour is observed upon gas adsorption. Chlorine adsorption on Cu(001) in an ordered $c(2 \times 2)$ overlayer for example did not quench this surface emission but lead to an energetic shift equal to the amount of work function change [41]. The same effect with opposite sign was observed for potassium adsorption on Pt(111) [47]. The most remarkable property of image potential states is therefore their pinning to the vacuum level of the sample. This is in fact in sharp contrast to bulk emission features which are uniquely referenced to the Fermi level.

4.5. The two-band model

In cases where surface states occur in gaps of sp bands and are sufficiently separated from the more localized d-states of the sample we may try a description of surface states in terms of nearly free electron wavefunctions similar to the bulk analysis in section 3 [48]. If we now introduce a surface at $z = 0$ and specify the reciprocal lattice vector in (12) to be normal to the surface, $\mathbf{G} = (0, 0, g)$, we obtain

$$V(z) = V_G [e^{igz} + e^{-igz}] = 2V_G \cos(gz), \quad z > 0, \quad g > 0, \quad (23)$$

and the trial function (13) becomes with $\mathbf{p} = (x, y)$

$$\psi_1 = \exp(i\mathbf{k}_{\parallel} \cdot \mathbf{p}) \{ a \exp(ik_z z) + b \exp[i(k_z - g)z] \}, \quad (24)$$

which satisfies Bloch's theorem now in two dimensions only. A graph of $V(z)$ is presented in fig. 15. If k_z is still restricted to be real we obtain of course the same energies as previously. Surface states with energies in the gap correspond to complex $k_z = \kappa + i\gamma$. If we introduce this complex k_z in (15) and equate the imaginary part of (15) to zero we find that for γ to be finite κ has to be $g/2$

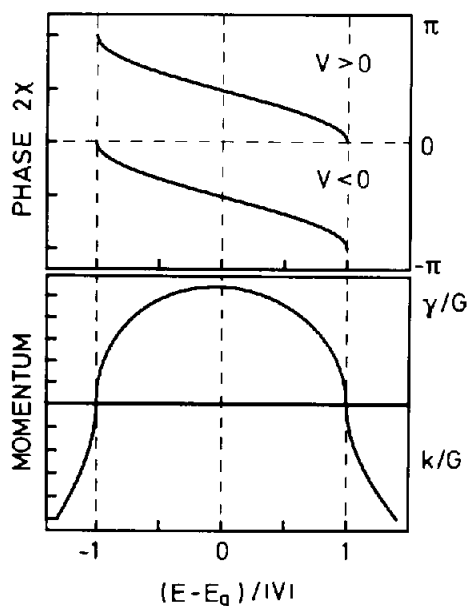


Fig. 16. Phase and momentum of the wavefunction in a bulk band gap.

convention adopted in fig. 15. In case of a rectangular surface potential barrier the wavefunction in the “forbidden” region will be

$$\psi \propto \exp(\gamma'z), \quad \gamma' > 0. \quad (29)$$

Equating the logarithmic derivatives of (26) and (29) at $z = z_0$ leads to

$$\gamma' = -\gamma - (g/2) \operatorname{tg}(gz_0/2 + \chi). \quad (30)$$

The periodicity of the potential restricts z_0 to the region between two atoms viz. $|z_0| < d/2$ where d is the interlayer spacing. A solution of (30) requires that $\operatorname{tg}(gz_0/2 + \chi) < 0$, in particular, for $z_0 = 0$, $V_G < 0$.

Among the many surfaces which exhibit surface states associated with an s-p band gap we mention the occupied surface states detected by angular resolved photoemission on the low index crystal faces of Cu [49–51]. They are all connected with the L_2 , L_1 band gap. Different projections of this gap can be seen from all three crystal surfaces.

Since γ , γ' and χ in (30) are all functions of energy, (30) determines the energetic position of the surface state. This depends still on the value of the unknown co-ordinate z_0 of the plane of wave matching, see fig. 15. Larsson and Nilsson were the first to use experimental photoemission data on occupied surface states on Cu and Ag to fit the parameter z_0 in calculations based on the one-step theory of photoemission. These parameters were then used to

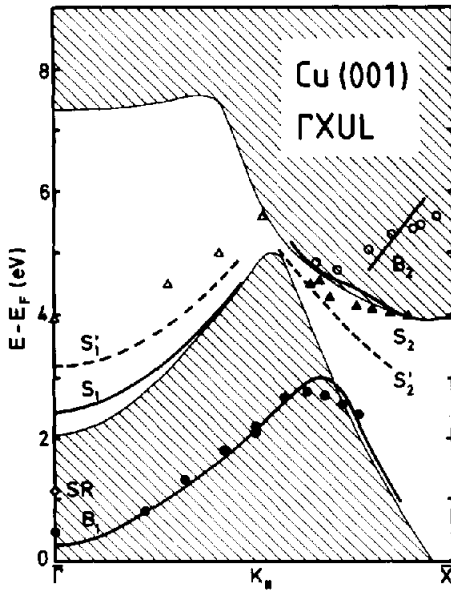


Fig. 17. Bulk band structure of Cu, projected onto the $\bar{\Gamma}\bar{X}$ direction of the surface Brillouin zone. Solid dots and open circles denote experimentally observed bulk direct transitions. Triangles show experimental results on surface state emission. The heavy lines are results from theoretical calculations, employing the one-step model of inverse photoemission. Dashed curves are for a different choice of the surface potential barrier.

predict empty surface states on Ni and Pd [52]. More recent results from the work of Thörner et al. [53] predict a surface state on Cu(001) at about 1.8 eV above the Fermi level. Vacuum level, Fermi level, potential depth and the X_4-X_1 band gap in fig. 15 are chosen to represent the situation on Cu(001) approximately. The surface state “SR” at 1.8 eV above E_F was obtained for $z_0 = +0.1d$. It is degenerate with bulk electronic states and represents therefore a surface resonance. The surface character of this state is best verified via its two-dimensional dispersion. In fact experimental data place this resonance at 1.1 eV above E_F and clearly show that the energetic position of the associated emission feature in an inverse photoemission spectrum remains stationary upon variation of the quantum energy for normally incident electrons, see feature SR in fig. 14. A complete set of inverse photoemission data for Cu(001) in the $\bar{\Gamma}\bar{X}$ bulk mirror plane obtained with a counter spectrometer at $\hbar\omega = 9.7$ eV is given in terms of $E(k_{||})$ in fig. 17 [54]. Solid dots and open circles labeled B_1 and B_2 , respectively, are bulk direct transitions closely analogous to B_2 , B_4 in fig. 6. Open and filled triangles show surface emissions and the diamond is the previously discussed surface resonance. The heavy solid and dashed curves S_1 , S_1' and S_2 , S_2' show the energy versus

momentum dispersion of the surface features from a one-step calculation. The position of the surface potential barrier was $z_0 = -0.05d$ for the continuous curves and $z_0 = +0.1d$ for the broken curves. While the observed surface state S_2 is quite well reproduced in energetic position and dispersion by suitable choice of z_0 , S_1 is only poorly represented. In fact the better the agreement for S_2 the worse the description of S_1 .

4.6. Surface potential barrier

The failure of a simple rectangular surface potential well to reproduce accurately all the observed surface state phenomena is by no means surprising. The interaction of an electron with a metal surface is asymptotically equal to the classical image potential. This is shown as the heavy solid line for $z < 0$ in fig. 15. Green's function theory, the standard approximation used to calculate the electron self-energy, shows that the image potential form is dominated by surface plasmon contributions in the response function of the solid [55]. The

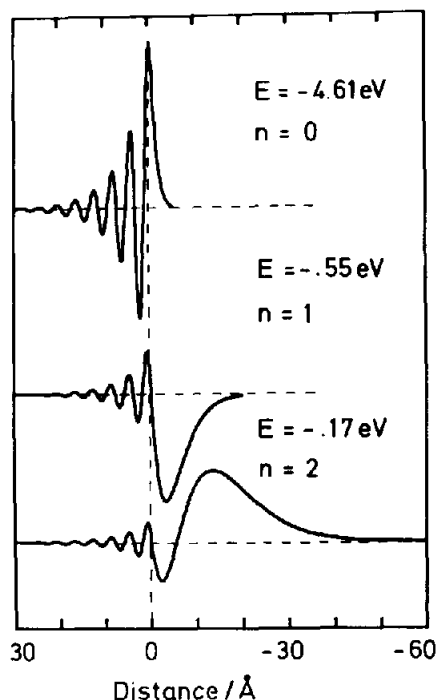


Fig. 18. Surface state wave functions for a coulombic surface potential barrier. The parameters of fig. 15 are chosen to represent the L-gap on Ag(111) and to match the occupied surface state observed in photoemission 4.61 eV below the vacuum level.

long range force of the image potential gives rise to a whole series of new surface states. Their energies can be obtained by integration of the one-dimensional Schrödinger equation in a Coulomb potential subject to the initial condition that the logarithmic derivative of the wavefunction should be equal to that of the gap wavefunction (26). The result of such a calculation is presented in fig. 18 [56]. The parameters were chosen to be $V_G = -2.3$ eV and $E_g - E_v = -2.4$ eV. These values are representative for the L-gap at Ag(111). The energetic position of the occupied surface state at $E - E_v = -4.61$ eV known from photoemission was then used to adjust the remaining parameter z_0 . The result was $z_0/d = +0.03$ which is nearly identical to the value obtained for a rectangular surface potential well. The relative insensitivity of this state to the shape of the surface potential barrier suggests the appellation "crystal derived". The wavefunction of this surface state is shown in the top part of fig. 18. The medium and lower trace are the wavefunctions associated with the first two new surface states introduced by the image potential with binding energies of 0.55 and 0.17 eV, respectively. We shall call these states "barrier derived" for obvious reasons. The wavefunctions are quite similar to the analytically soluble case

$$V(z) = \begin{cases} 1/4z, & z < 0, \\ \infty, & z > 0, \end{cases} \quad (31)$$

though the binding energies $E_1 = 0.85$ eV and $E_2 = 0.21$ eV are slightly different. The quantum number n indicates the number of nodes of the wavefunctions. An important message from fig. 18 is that the range of the wavefunction of the crystal derived state is significantly smaller than the range of the wavefunctions of the image potential states. This difference leads us to expect a widely different response of the respective surface states to surface contamination in accord with the observed insensitivity of the image potential states at Cu(001) and Pt(111) to adsorption of chlorine and potassium, respectively.

The small energetic separation between the ground state and excited states of the image potential prevents the observation of individual members of the Rydberg-like series by inverse photoemission in view of the presently available instrumental resolution. Instead we observe a step-like feature (see feature "S₁" in fig. 5) as a result of instrumental broadening. A high resolution technique for probing unoccupied electronic states in solids and at surfaces is two photon photoemission [57] where intense laser radiation is used to populate a normally empty state with the first photon and to photoionize from this intermediate state with the second photon. Image potential states are ideally suited as intermediate states, because a significant population can be built-up. This follows from their long lifetime which in turn is caused by their protrusion far out into the vacuum. Strong two photon photoemission from the occupied $n = 0$ surface state at Ag(111) with image potential states as inter-

mediates has recently been observed by Giesen et al. [58]. The 50 meV resolution of their apparatus was sufficient to resolve the $n=1$ and $n=2$ states at binding energies of (0.77 ± 0.03) eV and (0.23 ± 0.03) eV, respectively. The precise knowledge of the binding energies of several series members is needed for the construction of an even more realistic surface potential barrier.

4.7. Surface scattering formalism

An alternative description of the surface states discussed above can be obtained in the surface scattering formalism [59,60,26,61] which pictures electron waves being repeatedly reflected between the bulk crystal and the image potential barrier. If we denote the respective reflectivities by $r_C \exp(i\phi_C)$ and $r_B \exp(i\phi_B)$, bound states correspond to poles in the amplitude of

$$\psi^- = \{1 - r_C r_B \exp[i(\phi_B + \phi_C)]\}^{-1} \psi^+. \quad (32)$$

Poles in the amplitude of ψ^+ require that

$$r_C = r_B = 1, \quad (33)$$

and

$$\phi_B + \phi_C = 2\pi n. \quad (34)$$

Condition (33) can only be satisfied for energies below the vacuum level E_v ($r_B = 1$) in a bulk band gap ($r_C = 1$). The phase condition (34) on the other hand determines the energies of the surface states. The enumeration of the multiples of 2π corresponds to the previous classification of surface state wavefunctions in terms of their nodes.

4.8. Effective masses

Our discussion of image potential states has so far been restricted to $k_{\parallel} = 0$. For $k_{\parallel} \neq 0$ the nearly free electron two band approximation predicts a free-electron-like dispersion

$$E = \epsilon + \hbar^2 k_{\parallel}^2 / 2m. \quad (35)$$

Tables of binding energies and effective masses of image potential states have been prepared by Goldmann et al. [47] and Straub and Himpsel [62]. The effective masses tend to be considerably larger than one indicating the importance of lateral forces for $k_{\parallel} \neq 0$. The origin of such forces is quite clear. The image potential is a local and static description of the many particle screening response of the solid to the electron near its surface. Motion of the electron parallel to the surface will cause a concomitant propagation of the many body response. The “drag” associated with the propagation produces the retarding forces responsible for the observed effective masses.

5. Chemisorption

5.1. Adsorption at solid surfaces

The adsorption of atoms and molecules at solid surfaces continues to be the principal subject of research in surface science. Adsorption of an atom or molecule to a solid surface occurs when the total energy of the system is lowered upon formation of a bound state. Two types of adsorption, physisorption and chemisorption are usually distinguished. Though it has become customary to classify a system as either physisorbed or chemisorbed depending on the size of the adsorption energy we prefer a classification in terms of the nature of the binding force. Physisorption is then due to the Van der Waals dispersion force while chemisorption proceeds via an attractive exchange interaction. It follows that chemisorption forces unlike Van der Waals forces should be directed and specific not only for the particular adsorbate–substrate combination but also for the individual crystal face and adsorption site. Moreover, since exchange forces rest on a sharing of electrons between adsorbate and substrate, the electrons forming the chemisorption bond are always delocalized to a certain degree [63].

From a theoretical point of view chemisorption is an intermediate coupling problem in the sense that there is no obvious small expansion parameter in powers of which the solution could be constructed from a simple limiting case. It is therefore important in the course of development of a general theory of surface chemical bonding to understand in detail typical systems in terms of their electronic compositional and crystallographic microscopic parameters. Data on the energetic position and width of adsorbate induced unoccupied levels are a particularly valuable addition to our knowledge of chemisorption systems since all simple binding models start out with a consideration of the highest occupied and the lowest unoccupied energy levels.

5.2. Atomic chemisorption

Oxygen adsorption on Cu(110) has already been mentioned as a means of quenching surface states (see fig. 12). Simultaneously an emission feature due to oxygen induced empty electronic states develops at $E - E_F = 5$ eV which is associated with the $p(2 \times 1)$ adsorption geometry. Results from a similar study of oxygen adsorption on Ni(110) are shown in fig. 19 [64]. The spectra were taken for normally incident electrons. The clean surface exhibits only a weak emission peak at about 0.3 eV above E_F . This feature labeled B_1 can be identified with a bulk direct transition into an empty d-band just above E_F . Oxygen exposure leads to the growth of a new emission feature A_1 at $E - E_F = 3.2$ eV which is best developed for 0.8 L. LEED analysis showed that such an exposure leads to a well-ordered (2×1) superstructure. Upon further

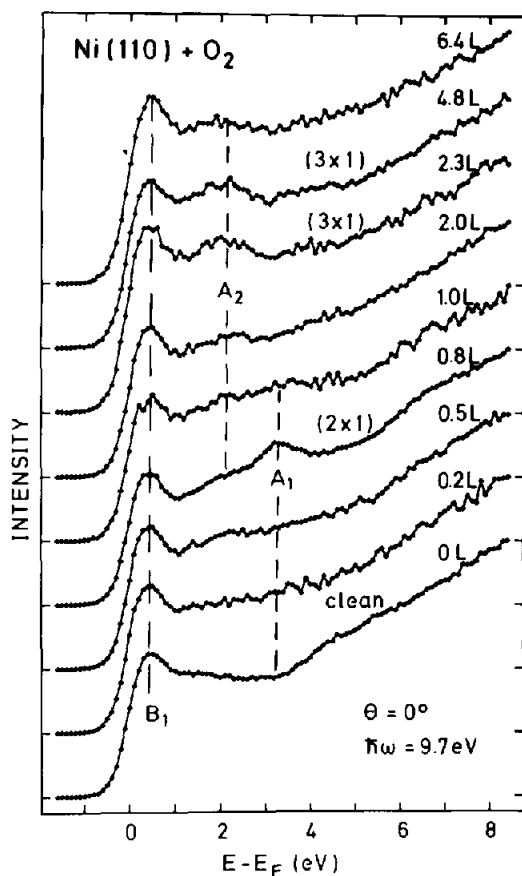


Fig. 19. Normal incidence isochromat spectra taken from Ni(110) as a function of oxygen exposure. Note that the energetic position of the adsorbate induced features depends on the adsorbate geometry.

oxygen exposure A_1 diminishes in intensity and a new emission feature A_2 appears at $E - E_F = 2$ eV. A_2 is most pronounced between 2.3 and 4.8 L. The LEED analysis reveals a (3×1) superstructure. More oxygen exposure leads again to an attenuation of A_2 and eventually to NiO formation. From a comparison of the Cu(110)/O data to the Ni(110)/O data we conclude that the energy of the oxygen derived state depends clearly on the substrate. Moreover from a comparison of the (2×1) and (3×1) adsorption geometries on Ni(110) we see that the energy of the oxygen derived empty state responds sensitively to different adsorption sites. This is of course also expected from different crystal faces. Fig. 20 shows inverse photoemission spectra for oxygen adsorbed at Ni(111) [65]. Panel a displays a series of normal incidence spectra

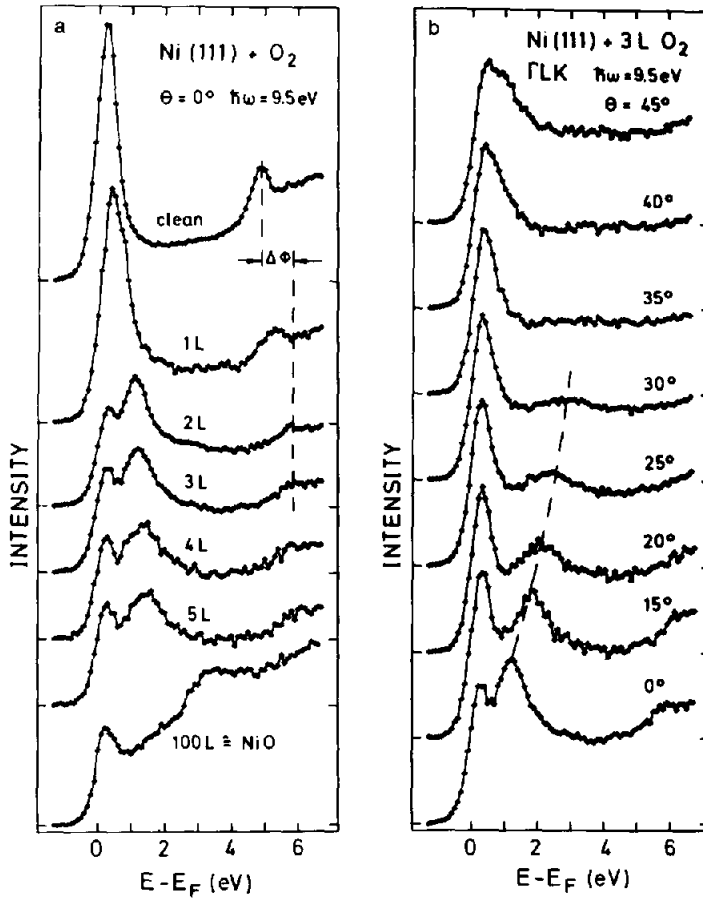


Fig. 20. The left panel shows normal incidence isochromat spectra from Ni(111) as a function of oxygen exposure. The right panel shows spectra demonstrating the dispersion of the adsorbate induced empty state for a $p(2 \times 2)$ overlayer along the Γ LK (Γ M) azimuth.

with the oxygen exposure as a parameter. A prominent oxygen derived emission feature shows up to 1.1 eV between 2 and 3 L. LEED analysis shows that exposures in this range lead to a sharp low background $p(2 \times 2)$ pattern. This is associated with a workfunction change of $\Delta\phi = (+0.9 \pm 0.2)$ eV as evidenced by the shift of the image potential emission. The bottom curve shows a characteristic example for NiO formation in the high exposure range [66,67]. Panel b of fig. 20 shows a series of spectra for 3 L exposure as a function of the angle of incidence of the primary electrons. The oxygen derived state exhibits considerable dispersion indicating substantial lateral interaction in the ordered oxygen overlayer. A plot of final state energy E_f as a function of

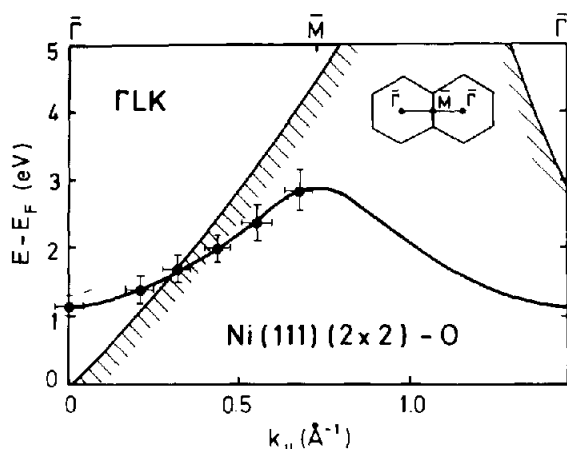


Fig. 21. Energy dispersion $E(k_{||})$ of the empty oxygen induced band on Ni(111)-p(2×2)-O along $\bar{\Gamma}\bar{M}$ of the adsorbate Brillouin zone. Unshaded areas indicate gaps of the projected bulk band structure.

$k_{||}$ shown in fig. 21 is seen to be fully compatible with the periodicity of the extended adsorbate zone scheme. This is suggested by the full line drawn through the experimental data points. From fig. 21 we see that the adsorbate derived band becomes degenerate with substrate bands already at small values of $k_{||}$. This may be responsible for the rapid intensity decrease of the oxygen derived emission feature since the degeneracy will lead to a shorter lifetime and associated broadening of the final electronic state.

Oxygen adsorbs on Ni(111) in a threefold hollow site. Electronic spectra do not, of course, reveal primarily structural information. However, dipole selection rules restrict optical transitions of normally incident electrons to final states of A_1 and A_3 symmetry. The polarization of the emitted radiation is linear parallel and perpendicular to the surface normal, respectively. Observation of the radiation at two different angles will then reveal polarization effects. Fig. 22 shows two spectra for normal electron incidence recorded under average observation angles of $\bar{\alpha} = 22^\circ$ and $\bar{\alpha} = 46^\circ$, respectively. For $\bar{\alpha} = 46^\circ$ one observes preferentially transitions to A_1 states while emission from A_3 states are enhanced at 22° . The difference between the observed emissions in the two geometries is shown in fig. 22b. It shows clearly that the image potential emission and the oxygen induced emission result from A_1 states while the peak at the Fermi energy results from transitions into A_3 -like d-bands. A localized view of the oxygen induced A_1 band, which is O(2p) derived, leads then to the orbital assignment p_z [65].

Facing the question what can be learnt from a knowledge of the energy versus momentum dispersion of unoccupied states induced by atomically

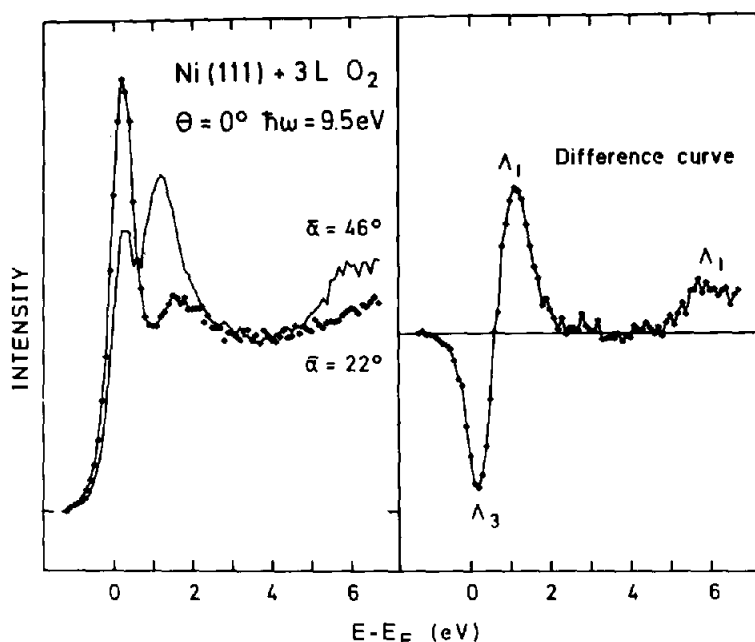


Fig. 22. The left panel shows normal incidence spectra from Ni(111)-p(2×2)-O taken at two different photon collection angles $\bar{\alpha}$. The difference curve in the right panel allows one to assign symmetry characters to the three emission features.

chemisorbed species, we must admit that we do not learn more than from spectra of occupied states. Moreover neither set of data provides a progress in the qualitative understanding of the chemisorption bond. It seems that real progress has to rely entirely upon extensive theoretical calculations. Such calculations are certainly in an encouraging state but further improvement is indispensable until we get predictions referring to particular adsorption faces and sites. Only such detailed theoretical results will advance our general understanding.

5.3. Molecular chemisorption

The vast amount of available photoemission data on molecular chemisorption has shown that these spectra are in certain respects easier to analyse than those from atomic chemisorption systems. The reason for this unexpected situation is that electronic states of adsorbed molecules appear to remain rather localized and retain much of their gas phase character. A beautiful demonstration of this behaviour is presented in the early data on benzene adsorbed on Ni(111) by Demuth and Eastman [68]. Data like these were

milestones in establishing the “fingerprint technique” which was later on even employed to identify surface reactions such as the dehydrogenation of chemisorbed ethylene to acetylene on Ni(111).

Molecules like benzene are already quite complicated from the point of view of basic research and the majority of chemisorption experiments has therefore dealt with simple diatomic molecules such as CO, NO, N₂, and O₂. In particular carbon monoxide has developed as the preferential working horse for chemisorption studies and it was quite natural to employ the new technique of inverse photoemission to this class of problems also.

Carbon monoxide is bound to most metal surfaces via the carbon end and is oriented parallel to the surface normal. The special interest in inverse photoemission studies of CO adsorbed in such a geometry stems from the prominent role assigned to the lowest unoccupied 2π molecular orbital in the chemisorption bond. Within Blyholder's model [69] the bonding of CO to metal surfaces arises through donation from the occupied 5σ molecular orbital to the metal substrate and charge backdonation from the metal to the previously empty 2π orbital. A recent theoretical study [70] concludes that 2π backdonation is by far the more important part of the two contributions to the bond. Within a highly simplified picture the CO interaction with a d-band metal leads then to the formation of π states which are linear combinations of CO 2π and metal d_π states

$$|\pi\rangle = \alpha|2\pi\rangle_{\text{CO}} + \beta|d_\pi\rangle_{\text{metal}}. \quad (36)$$

While one of these linear combinations is mainly of metal d-parentage and therefore nearly occupied the other is of predominant CO-parentage and therefore nearly empty and readily accessible by inverse photoemission spectroscopy. Though the CO 2π level is an essential bonding ingredient for the molecule surface bond, it is antibonding with respect to the intramolecular C–O bond. We will discuss these two aspects in slightly more detail below.

The first inverse photoemission study of CO adsorption was reported by Fauster and Himpsel for Ni(111) [71]. Fig. 23 presents a sample of their data taken at an initial state energy of 20 eV for various angles of incidence for a clean and CO covered nickel sample. We note from fig. 23 an attenuation of the substrate d-band emission and the emergence of a new broad peak at 3 eV above E_F upon CO adsorption. This extra emission is due to the 2π derived empty electronic state of the chemisorption system. It does not show dispersion. However, in view of the normal orientation of CO on Ni(111) for saturation coverage, the observed intensity variation with increasing angle of incidence of the primary electrons (see the geometry sketched in fig. 23) has been used to assign a predominant $p_{x,y}$ character to the 2π induced empty state.

Many other molecule substrate combinations have been investigated after this pioneering study. As an example we shall discuss briefly the adsorption of

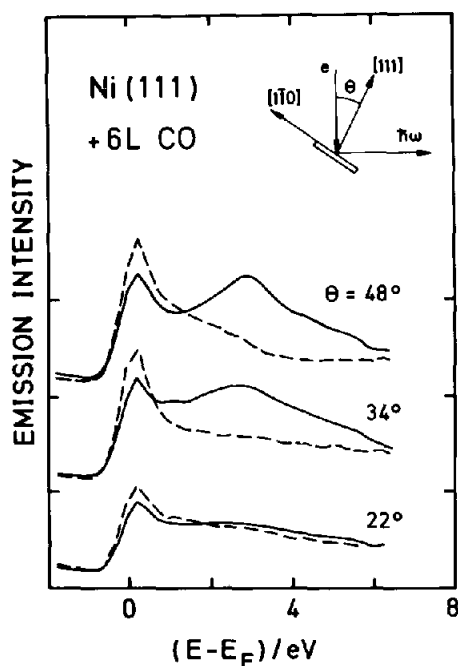


Fig. 23. Inverse photoemission spectra at 20 eV initial state energy E_i from a clean (dashed line) and CO covered (solid line) Ni(111) surface for various angles of incidence. The experimental geometry is sketched in the upper right corner [71].

CO and NO on Pd(100) [72]. The left-hand panel of fig. 24 shows spectra at 9.7 eV photon energy from clean and CO covered Pd(100). The clean surface spectrum exhibits emission features from transitions into empty d-bands close to the Fermi level and a direct interband transition at 3 eV above E_F in close analogy to the nickel spectra in fig. 5. Both emission features of the clean substrate are attenuated upon CO adsorption but, more important, a prominent new emission from transitions into CO 2π derived states of the chemisorption system grows at about 4.5 eV. Before turning to the NO case, let us recall that the 2π level of gaseous CO is completely empty while that of NO is singly occupied resulting in a markedly lower dissociation energy. The right-hand panel of fig. 24 shows inverse photoemission spectra for NO adsorbed on Pd(100). The NO induced extra emission develops at 1.5 eV above E_F in this case. Its position can be more easily identified for an angle of incidence of $\theta = 30^\circ$ since the bulk interband transition has dispersed to higher energy in this case. The observed energetic position of the NO derived π state close to the Fermi energy in the Pd/NO system facilitates the backdonation mechanism (larger β in eq. (36)) as compared to CO and explains in quite a natural

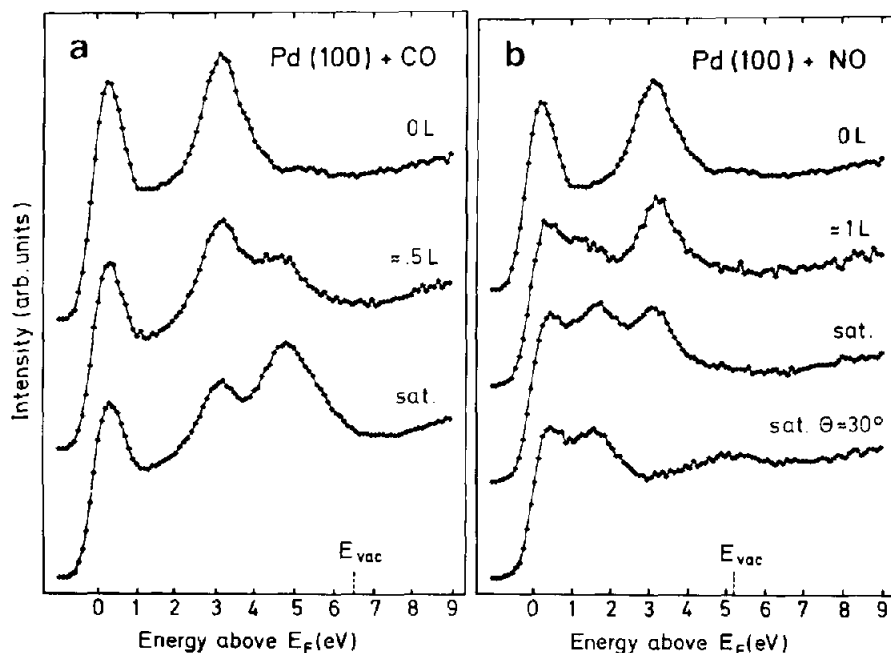


Fig. 24. Bremsstrahlung isochromat spectra at 9.7 eV photon energy from a clean Pd(100) surface and after CO (left panel) and NO (right panel) adsorption.

way the known higher tendency of NO to dissociate upon adsorption to metal surfaces.

In an attempt to summarize the available inverse photoemission data for the adsorption of CO on various metal surfaces the energetic position of the 2π derived state relative to the vacuum level has been plotted in the lower panel of fig. 25 as a function of the desorption temperature. If the desorption temperature is taken as an – admittedly – coarse measure of the energy of the surface–molecule bond, the diagram reveals that the lowering of the 2π level below the vacuum level correlates well with the energy of the chemisorption bond and hence with the amount of backdonation. We mentioned already, that charge backdonation to the 2π level is expected to weaken the intramolecular bond. A certain measure of the intramolecular binding strength is provided by the C–O stretch frequency measured in high resolution electron energy loss spectroscopy (HREELS). The energy of this intramolecular vibration is displayed in the upper panel of fig. 25 and seems to suggest that in fact a strengthening of the chemisorption bond occurs on account of the intramolecular bonding strength. Some reservation on this statement is in order. The intramolecular stretch frequency depends not only on the depth of the in-

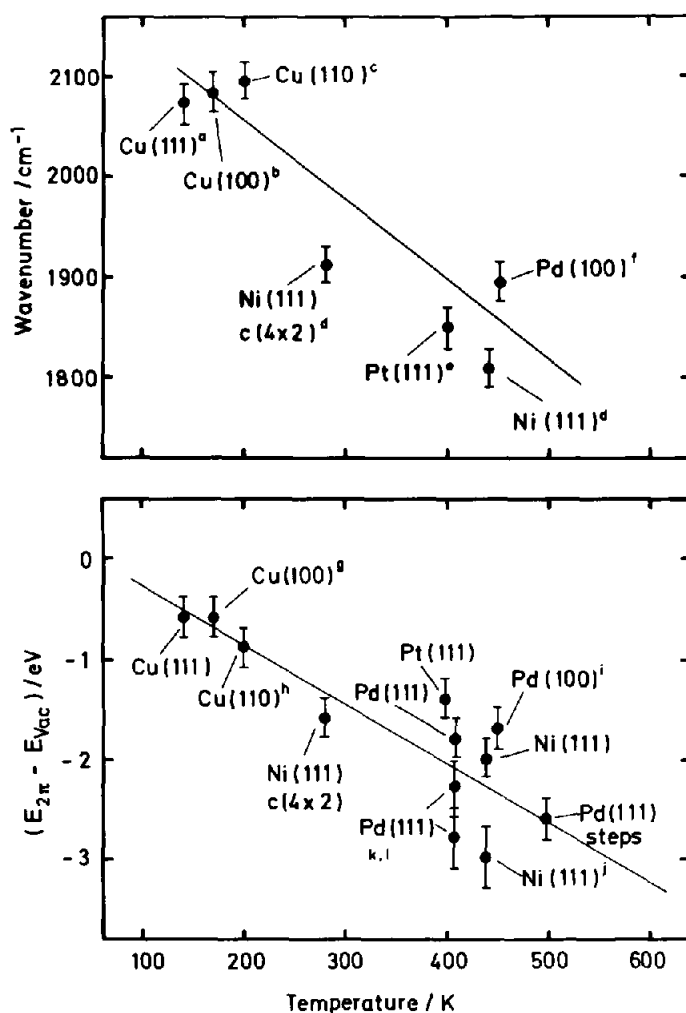


Fig. 25. The lower panel shows the energetic position of the CO 2 π level relative to the vacuum level as a function of the desorption temperature for various metal surfaces. The upper panel displays the energy of the C-O stretch frequency as a function of the desorption temperature.

tramolecular potential but also on its width. While HREELS discriminates clearly between different binding sites, for example “on top” and “bridge” sites on Pt(111), inverse photoemission data have so far failed to identify different electronic levels in the two geometries. The vibrational data for Pd and Pt in fig. 25 refer to bridge sites only.

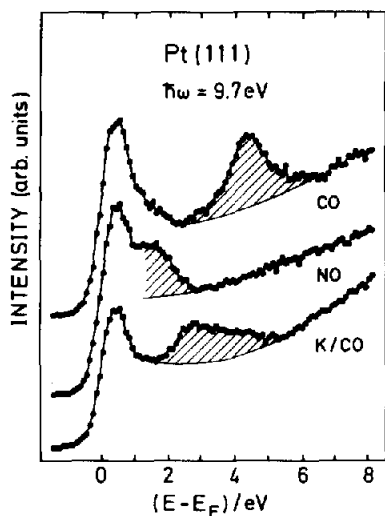


Fig. 26. Bremsstrahlung isochromat spectrum from a CO covered K-promoted Pt(111) surface in comparison to spectra for CO and NO adsorption on unpromoted Pt(111).

5.4. CO adsorption

Great current interest focuses on CO adsorption on alkali promoted metal surfaces. The general interest in such coadsorption systems derives from the well-known and poorly understood behaviour of technical catalysts which speed up selectively certain heterogeneous catalytic reactions upon addition of small amounts of alkali compounds [73]. A similar dramatic change of the chemisorptive properties is known for CO adsorption on well-ordered single crystal surfaces pre-exposed to small amounts of alkali metals. Inverse photoemission studies of CO coadsorbed with potassium are just becoming available. As an example which is meant to give a taste of the results to be expected fig. 26 presents spectra for CO/K on Pt(111). Spectra for NO on Pt(111) and CO on Pt(111) have been added for comparison. The energetic position of the 2π derived level on the potassium promoted platinum surface occurs midway between the CO and NO cases. This indicates that the promotional effect of potassium proceeds via enhanced backdonation to the molecular 2π level which in turn leads to a strengthening of the molecule substrate bond and a weakening of the intramolecular bond. This conclusion is in keeping with increased desorption temperatures and decreased vibrational energies observed for CO on K promoted Pt(111) [74,75]. In view of the drastic energetic shifts exhibited by the 2π derived unoccupied states as compared to the occupied 5σ and 1π molecular orbitals observed in photoemission we dare forecast that inverse photoemission studies of CO/K coadsorption as a function of CO

and/or K coverage will significantly advance our understanding of the alkali promotional effect in heterogeneous catalysis.

Acknowledgements

The author wishes to acknowledge his co-workers for their contribution to this article and for permission to include also data which have not yet been published elsewhere. I am indebted to C. Benndorf, G. Borstel and A. Goldmann for critical readings of the manuscript. M. Donath has been very helpful with the references and Mrs. M. Lukacs has again done an expert job in preparing the figures. Continuous financial support by the Deutsche Forschungsgemeinschaft is reflected in the various experimental data from our own laboratory included in this report.

References

- [1] W.C. Röntgen, Sitz. Ber. Med. Phys. Ges. Würzburg, 137 (1895).
- [2] W. Heitler, *The Quantum Theory of Radiation*, 3rd ed. (Clarendon, Oxford, 1954).
- [3] G.W. Gobeli, F.G. Allen and E.O. Kane, *Phys. Rev. Letters* 12 (1964) 94.
- [4] F.J. Himpsel, *Advan. Phys.* 32 (1983) 1.
- [5] V. Dose, *Progr. Surface Sci.* 13 (1983) 225; *J. Phys.Chem.* 88 (1984) 1681; *Appl. Surf. Sci.* 22/23 (1985) 338; *Festkörperprobleme XXV* (1985) 555.
- [6] D.P. Woodruff, P.D. Johnson and N.V. Smith, *J. Vacuum Sci. Technol.* A1 (1983) 1104.
- [7] F.J. Himpsel, *Comments Solid State Phys.*, to be published;
F.J. Himpsel and Th. Fauster, *J. Vacuum Sci. Technol.* A2 (1984) 815.
- [8] N.V. Smith, *Vacuum* 33 (1983) 803; *Appl. Surface Sci.* 22/23 (1985) 349.
- [9] P.O. Nilsson and A. Kovacs, *Phys. Scripta* T4 (1983) 61.
- [10] Th. Fauster and V. Dose, in: *Inverse Photoemission Spectroscopy*, Vol. 6 of *Chemistry and Physics of Solid Surfaces*, Ed. R. Vanselow (Springer, Berlin, 1986).
- [11] E.A. Milne, *Phil. Mag.* 47 (1924) 209.
- [12] J.B. Pendry, *Phys. Rev. Letters* 45 (1980) 1356.
- [13] J.B. Pendry, *J. Phys. C (Solid State Phys.)* 14 (1981) 1381.
- [14] J.K. Lang and Y. Baer, *Rev. Sci. Instr.* 50 (1979) 221.
- [15] G. Chauvet and R. Baptist, *J. Electron Spectrosc. Related Phenomena* 24 (1981) 255.
- [16] Th. Fauster, F.J. Himpsel, J.J. Donelon and A. Marx, *Rev. Sci. Instr.* 54 (1983) 68.
- [17] V. Dose, *Appl. Phys.* 14 (1977) 117.
- [18] G. Denninger, V. Dose and H. Scheidt, *Appl. Phys.* 18 (1979) 375.
- [19] A. Goldmann, M. Donath, W. Altmann and V. Dose, *Phys. Rev.* B32 (1985) 837.
- [20] V. Dose, M. Glöbl and H. Scheidt, *Phys. Rev.* B30 (1984) 1045.
- [21] K. Desinger, V. Dose, M. Glöbl and H. Scheidt, *Solid State Commun.* 49 (1984) 479.
- [22] J.A.R. Samson, *Techniques of Vacuum Ultraviolet Spectroscopy* (Wiley, New York, 1967).
- [23] G. Denninger, V. Dose and H.P. Bonzel, *Phys. Rev. Letters* 48 (1982) 279.
- [24] J. Rogozik, H. Scheidt, V. Dose, K.C. Prince and A.M. Bradshaw, *Surface Sci.* 145 (1984) L481.
- [25] T.T. Childs, W.A. Royer and N.V. Smith, *Rev. Sci. Instr.*, to be published.
- [26] S.L. Hulbert, P.D. Johnson, N.G. Stoffel, W.A. Royer and N.V. Smith, *Phys. Rev.* B31 (1985) 6815.
- [27] M. Wöhlecke, A. Baalman and M. Neumann, *Solid State Commun.* 49 (1984) 217.

- [28] D.P. Woodruff, N.V. Smith, P.D. Johnson and W.A. Royer, *Phys. Rev. B* 26 (1982) 2943.
- [29] E.O. Kane, *Phys. Rev. Letters* 12 (1964) 97.
- [30] G. Borstel, *Appl. Phys. A* 38 (1985) 193.
- [31] G. Thörner and G. Borstel, *Solid State Commun.* 49 (1984) 997.
- [32] V.L. Moruzzi, J.F. Janak and A.R. Williams, *Calculated Electronic Properties of Metals* (Pergamon, New York, 1978).
- [33] N.V. Smith and L.F. Matheiss, *Phys. Rev. B* 9 (1974) 1341.
- [34] D. Straub, M. Skibowski and F.J. Himpsel, *Phys. Rev. B* 32 (1985) 5237.
- [35] Th. Fauster, F.J. Himpsel, J.E. Fischer and E.W. Plummer, *Phys. Rev. Letters* 57 (1983) 430.
- [36] D. Straub, M. Skibowski and F.J. Himpsel, *Phys. Rev. B* 31 (1985) 8254.
- [37] I. Tamm, *Z. Phys.* 76 (1932) 848.
- [38] W. Shockley, *Phys. Rev.* 56 (1939) 317.
- [39] P.D. Johnson and N.V. Smith, *Phys. Rev. Letters* 49 (1982) 290.
- [40] D.A. Wesner, P.D. Johnson and N.V. Smith, *Phys. Rev. B* 30 (1984) 503.
- [41] V. Dose, W. Altmann, A. Goldmann, U. Kolac and J. Rogozik, *Phys. Rev. Letters* 52 (1984) 1919.
- [42] D. Straub and F.J. Himpsel, *Phys. Rev. Letters* 52 (1984) 1922.
- [43] P.D. Johnson and N.V. Smith, *Phys. Rev. B* 27 (1983) 2527.
- [44] H. Scheidt, M. Glöbl, V. Dose and J. Kirschner, *Phys. Rev. Letters* 51 (1983) 1688.
- [45] B. Reihl, K.H. Frank and R.R. Schlittler, *Phys. Rev. B* 30 (1984) 7328.
- [46] D. Straub and F.J. Himpsel, to be published.
- [47] A. Goldmann, V. Dose and G. Borstel, *Phys. Rev. B* 32 (1985) 1971.
- [48] F. Forstmann, *Z. Phys.* 235 (1970) 69.
- [49] P.O. Gartland and B.J. Slagvold, *Phys. Rev. B* 12 (1975) 4047.
- [50] S.D. Kevan, *Phys. Rev. Letters* 50 (1983) 526.
- [51] S.D. Kevan, *Phys. Rev. B* 28 (1983) 2268.
- [52] C.G. Larsson and P.O. Nilsson, *Phys. Letters* 85A (1981) 393.
- [53] G. Thörner, G. Borstel, V. Dose and J. Rogozik, *Surface Sci.* 157 (1985) L379.
- [54] V. Dose, U. Kolac, G. Borstel and G. Thörner, *Phys. Rev. B* 29 (1984) 7030.
- [55] J.C. Inkson, *Surface Sci.* 28 (1971) 69.
- [56] G. Borstel, G. Thörner, V. Dose and R. Schneider, *Surface Sci.*, to be published.
- [57] H.W. Rudolf, D. Rieger and W. Steinmann, *Solid State Commun.* 34 (1980) 427.
- [58] K. Giesen, F. Hage, F.J. Himpsel, H.J. Riess and W. Steinmann, *Phys. Rev. Letters* 55 (1985) 300.
- [59] P.M. Echenique and J.B. Pendry, *J. Phys. C* 11 (1978) 2065.
- [60] E.G. McRae, *Rev. Mod. Phys.* 51 (1979) 541.
- [61] R.F. Garret and N.V. Smith, *Phys. Rev. B*, to be published.
- [62] D. Straub and F.J. Himpsel, *Phys. Rev. B*, to be published.
- [63] J.R. Smith, Ed., *Theory of Chemisorption*, Vol. 19 of *Topics in Current Physics* (Springer, Berlin, 1980).
- [64] K. Desinger, V. Dose, A. Goldmann, W. Jacob and H. Scheidt, *Surface Sci.* 154 (1985) 695.
- [65] W. Altmann, K. Desinger, M. Donath, V. Dose, A. Goldmann and H. Scheidt, *Surface Sci.* 151 (1985) L185.
- [66] H. Scheidt, M. Glöbl and V. Dose, *Surface Sci.* 112 (1981) 97.
- [67] V. Dose, M. Glöbl and H. Scheidt, *J. Vacuum Sci. Technol. A* 1 (1983) 1115.
- [68] J.E. Demuth and D.E. Eastman, *Phys. Rev. Letters* 32 (1974) 1123.
- [69] G. Blyholder, *J. Phys. Chem.* 68 (1964) 2772.
- [70] P.S. Bagus, C.J. Nelin and Ch.W. Bauschlicher, *Phys. Rev. B* 28 (1983) 5423.
- [71] Th. Fauster and F.J. Himpsel, *Phys. Rev. B* 27 (1983) 1390; *Phys. Rev. Letters* 49 (1982) 1583.
- [72] J. Rogozik, J. Küppers and V. Dose, *Surface Sci.* 148 (1984) L653.
- [73] H.P. Bonzel, *J. Vacuum Sci. Technol. A* 2 (1984) 866.
- [74] E.L. Garfunkel, J.E. Crowell and G.A. Somorjai, *J. Phys. Chem.* 86 (1982) 310.
- [75] M. Kiskinova, G. Pirug and H.P. Bonzel, *Surface Sci.* 133 (1983) 321.